George Z. Voyiadjis · **Rick Peters**

Size effects in nanoindentation: an experimental and analytical study

Abstract This work addresses the size effect encountered in nanoindentation experiments. It is generally referred to as the indentation size effect (ISE). Classical descriptions of the ISE show a decrease in hardness for increasing indentation depth. Recently new experiments have shown that after the initial decrease, hardness increases with increasing indentation depth. After this increase, finally the hardness decreases with increasing indentation. This work reviews the existing theories describing the ISE and presents new formulations that incorporate the hardening effect into the ISE. Furthermore, indentation experiments have been performed on several metal samples, to see whether the hardening effect was an anomaly or not. Finally, numerical simulations are performed using the commercial program ABAQUS.

1 Introduction

In this work, size effects are investigated by studying macro- to nanoindentation of several metal samples. This is referred to as the indentation size effect (ISE). The existence of the ISE has been widely proven in the literature [1–3] (see Fig. 1). The ISE manifests itself in nanoindentation experiments, at small indentation depths h. For these small values of h, the material appears to be harder than at larger indentation depths. Indenting up to larger depths eventually results in measuring the macrohardness H_0, which is acquired by performing classical macroindentation tests.

The ISE cannot be captured using classical continuum theory; the classical theory is only able to predict the macrohardness H_0. A gradient theory is used to bridge the gap between the macro- and the micro/nano-scale. Associated with this gradient theory is a material intrinsic length scale l, which is used to characterize the ISE for different metals.

Using this gradient theory, an expression which describes the hardness as a function of indentation depth can be derived. Combining this expression with results acquired from nanoindentation experiments, a value for the material intrinsic length scale l can be determined.

Recently, new experiments have indicated a hardening effect accompanying the ISE [4]. Instead of hardness solely decreasing for increasing indentation depth, one also notes a region, at very small depths, that experiences increasing hardness for increasing indentation depth. For the smallest indentation depths, it is observed that the hardness decreases. However, it is also observed that for increasing indentation depths, the hardness suddenly increases. Further increasing the indentation depth again yields a decreasing hardness, as shown in Fig. 2.

G. Z. Voyiadjis (✉)
Department of Civil and Environmental Engineering, Louisiana State University, Baton Rouge, LA 70803, USA
E-mail: voyiadjis@eng.lsu.edu

R. Peters
Department of Mechanical Engineering, Eindhoven University of Technology, Eindhoven, The Netherlands
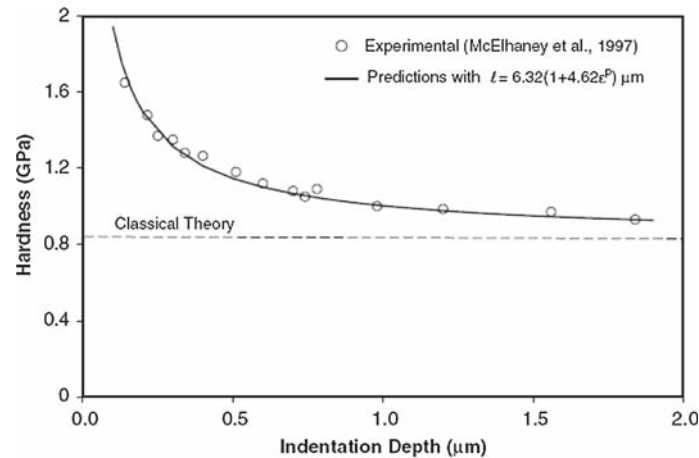
Fig. 1 Visualization of the ISE: hardness decreases with increasing indentation depth. This particular plot is a fit of the ISE gradient model to experimental results versus classical continuum theory [3]
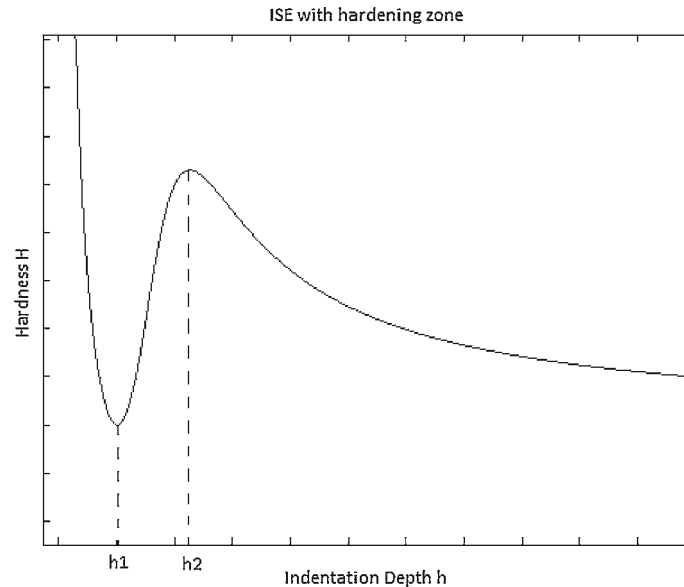
Fig. 2 Visualization of the ISE with the incorporated hardening effect. For $h < h_1$, hardness decreases, for $h_1 < h < h_2$, hardness increases and for $h > h_2$, hardness decreases again

An empirical relation has been developed [4] to incorporate this hardening effect in the ISE.

The aim of this work is to repeat these experiments with smooth surfaces, to see whether the hardening effect is an anomaly or not. The preparation, execution and results of these experiments will be described in this work.

Furthermore an attempt is made to derive a physically based expression to describe the ISE with the incorporated hardening effect. Finally, the experiments will be simulated numerically with the ABAQUS commercial program. This is to ascertain values for the plastic equivalent strain during the indentation process.

2 The MTS nanoindenter XP

The instrument used to perform the nanoindentation tests is the nanoindenter XP, developed by MTS. It uses high-tech control electronics and depth sensing techniques. This way it is able to determine the material hardness H and the elasticity modulus E. A diamond Berkovich tip is used to make the indents. During one test run the user can instruct the machine to make an array of indents, for instance a 4×4 array, which will yield

16 sets of data. An average for these 16 sets will be determined and sets with extremely different results can be identified and eliminated. To exclude environmental interference like heat generation and vibrations, the machine corrects for thermal drift and uses air bearings to stabilize its base, respectively.

To ensure the consistency of the tests performed on a certain sample, a test run is made on standard fused silica before and after the actual sample test. The elastic modulus of standard fused silica is well known ($E = 72\,\text{GPa}$) and the material is ideal to use for this purpose. If the results of one of the test-runs deviate significantly, the test of the actual sample will probably be corrupted.

The actual working principle of the machine is based on a series of equations, developed by Oliver and Pharr [5]. The first basic equation is the one that determines the hardness H of the material

$$H = \frac{P}{A}.$$
(1)

In this equation, H is the hardness in Pascal, P is the load that the indenter applies on the sample in Newton and A is the contact surface area between the indenter tip and sample in m^2.

During the indentation test the strain rate $\dot{\varepsilon}$ remains constant at 0.05 (1/s). This implies that the load P changes during the test,

$$P = B \left(h - h_f \right)^m.$$
(2)

In this equation, B and m are empirically determined fitting parameters, h_f is the final displacement in meters after complete unloading and h is the indentation depth in meters.

The contact surface A can be written as a function of the contact depth h_c:

$$A = f(h_c).$$
(3)

This function is known for the Berkovich tip which is used in this work. However, h_c has to be determined in order to evaluate the function:

$$h_c = \frac{h - \varepsilon P}{S}.$$
(4)

In this equation, ε is a constant dependant on the tip geometry (for Berkovich $\varepsilon = 0.75$). Furthermore S is the slope of the initial portion of the unloading curve. The slope S is obtained by differentiating the contact load P with respect to the indentation depth h,

$$S = \frac{\mathrm{d}P}{\mathrm{d}h} = Bm \left(h - h_f \right)^{m-1} \Big|_{h=h_{\max}}.$$
(5)

In this equation, $h_{\max}$ is the maximal indentation depth reached during the test. Using these equations the machine can determine the hardness H of the material as a function of the indentation depth h. The machine is also able to determine the elastic modulus E of the tested sample. The modulus E follows from the following expression for the reduced modulus E_r (Pa):

$$\frac{1}{E_r} = \frac{(1 - v^2)}{E} + \frac{(1 - v_i^2)}{E_i}.$$
(6)

Here E is the modulus of elasticity of the sample, v is the corresponding Poisson ratio, E_i is the indenter modulus of elasticity ($E_i = 1{,}141\,\text{GPa}$), v_i is the indenter Poisson ratio ($v_i = 0.07$) and E_r is the reduced modulus of elasticity. The expression for E_r is given by

$$E_r = \frac{\sqrt{\pi}\,S}{2\beta\sqrt{A}}.$$
(7)

Here β is a constant dependant on the indenter geometry. For Berkovich the constant is given as $\beta = 1.034$.

3 Gradient plasticity theory and material intrinsic length scale

As indicated in Sect. 1, the classical continuum plasticity needs to be enhanced using ISE in order to introduce micromechanical plasticity in the constitutive modeling and address multiscale characterization in the material behavior. The enhanced strain–gradient plasticity theories formulate a constitutive framework on the continuum level that is used to bridge this gap. To assess the size effects, an intrinsic material length scale parameter is incorporated into the constitutive equations.

The ISE and size effects in metals may be characterized using statistically stored dislocations (SSDs) and geometrically necessary dislocations (GNDs) and their interactions. Material hardening is caused by dislocation storage and it is generally believed that size affects arise from an increase in strain gradients inherent in small localized zones. This in turn leads to the emerging of GNDs that cause additional hardening by acting as obstacles to the SSDs.

The SSDs are dislocations moving through the material and trapping each other in a random way. The GNDs are dislocations that are required for compatible deformation within the polycrystal. In other words, they are required to accommodate the crystal-lattice curvature that arises whenever there is a non-uniform plastic deformation. In general SSDs are related to equivalent plastic strain and GNDs are related to strain gradients. In indentation, GNDs arise because of the material being pushed into the underneath substrate material by the indenter and getting stored as GNDs (see Fig. 3). To generalize this, non-uniform deformation will give rise to an extra storage of material defects (to be called GNDs) in comparison with uniform deformation at the same strain level. The GNDs manifest their effects when the characteristic length of deformation becomes sufficiently small.

In this work, a gradient plasticity theory developed by Voyiadjis and Abu Al-Rub [2] will be used, which will be outlined below.

Gradient plasticity is introduced through the non-local weak formulation of the conventional effective plastic strain. In general the non-local form $\hat{p}$ is written in terms of its local counterpart p and high-order gradient terms.

$$\hat{p} = \left[p^\gamma + (l\eta)^\gamma \right]^{1/\gamma} . \tag{8}$$

Here l is the length scale parameter that is required for dimensional consistency. In Eq. (8), p is the effective plastic strain and η is the effective plastic strain gradient of any order. The constant γ is a material parameter.

The Taylor flow stress is used to define the critical shear stress that is required to untangle the interactive dislocations and to introduce a significant plastic deformation:

$$\tau = \left[\tau_S^\beta + \tau_G^\beta \right]^{1/\beta} , \tag{9}$$

where τ_S and τ_G are given by the Taylor's hardening laws related to the SSD density (ρ_S) and GND density (ρ_G):

$$\tau_S = \alpha_S G b_S \sqrt{\rho_S}, \tag{10}$$
$$\tau_G = \alpha_G G b_G \sqrt{\rho_G}, \tag{11}$$

where b_S and b_G are the magnitudes of the Burgers vectors for the SSDs and GNDs respectively, G is the shear modulus and α_S and α_G are statistical coefficients which account for the deviation from regular spatial
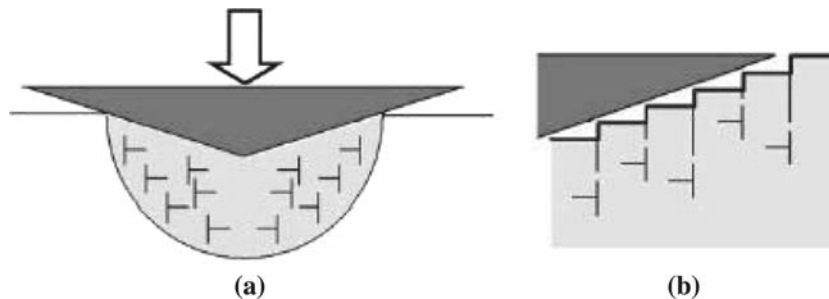

Fig. 3 a Material is being pushed by the indenter into the underlying substrate material, with an extra storage of defects (GNDs) as effect. **b** Detailed view of the deformation on atomic level and the associated GNDs [6]

arrangements of the SSD and GND populations respectively. Finally, β is a constant material parameter (used for fitting).

Substituting Eqs. (10) and (11) into Eq. (9) yields a general expression for the overall flow stress in terms of an equivalent total dislocation density, ρ_T:

$$\tau = \alpha_S G b_S \sqrt{\rho_T}, \tag{12}$$

and

$$\rho_T = \left[\rho_S^{\beta/2} + \left(\alpha_G^2 b_G^2 \rho_G / \alpha_S^2 b_S^2 \right)^{\beta/2} \right]^{2/\beta}. \tag{13}$$

Equation (12) is set at the microscale, however, plasticity is the macroscopic outcome from the combination of many dislocation properties at the micro- and mesoscopic scales. The flow stress can be written at the macroscopic level using a power law ($\sigma = k \hat{p}^{1/m}$), and combining this with Eq. (8) yields

$$\sigma = k \left[p^\gamma + l^\gamma \eta^\gamma \right]^{1/m\gamma}, \tag{14}$$

where $\gamma, k,$ and m are material constants.

The non-local effects associated with the presence of local deformation gradients at a given material point are incorporated into Eq. (13) through the GND density ρ_G and into Eq. (14) through the strain gradient η.

The gradient in the plastic strain field is accommodated by the GND density ρ_G so that the effective strain gradient η introduced in Eq. (8) can be defined as

$$\eta = \frac{\rho_G b_G}{\bar{r}}, \tag{15}$$

where $\bar{r}$ is the Nye factor [7,8].

The plastic shear strain γ^p can be defined as a function of the SSD density ρ_S as follows:

$$\gamma^p = b_S L_S \rho_S, \tag{16}$$

where L_S is the mean spacing between SSDs which is usually in the submicron order. The plastic strain in the macroscopic plasticity theory is defined in terms of the plastic shear strain γ^p as

$$\varepsilon_{ij}^p = \gamma^p M_{ij}, \tag{17}$$

where M_{ij} is the symmetric Schmidt's orientation tensor.

The flow stress σ is the conjugate of the effective plastic strain variable p in macro-plasticity. For proportional, monotonically increasing plasticity, p is defined as

$$p = \sqrt{2\varepsilon_{ij}^p \varepsilon_{ij}^p / 3}. \tag{18}$$

Combining Eqs. (16) and (17) and substituting the result into Eq. (18) gives p as a function of SSD density as follows:

$$p = b_S L_S \rho_S \bar{M}, \tag{19}$$

with

$$\bar{M} = \sqrt{2 M_{ij} M_{ij} / 3}. \tag{20}$$

Here $\bar{M}$ is the Schmidt's orientation factor, usually taken equal to 1/2.

Rewriting Eqs. (15) and (19) for ρ_G and ρ_S, respectively, and substituting them in Eqs. (12) and (13) yields an expression for τ. Combining this expression with $\sigma = \sqrt{3}\tau$ finally yields the flow stress:

$$\sigma = \alpha_S G \sqrt{3 b_S / L_S \bar{M}} \left[p^{\beta/2} + \left(\alpha_G^2 b_G L_S \bar{M} \bar{r} / \alpha_S^2 b_S \right)^{\beta/2} \eta^{\beta/2} \right]^{1/\beta}. \tag{21}$$

Comparing Eqs. (14) and (21) yields the following expressions:

$$\gamma = \frac{\beta}{2}, \tag{22}$$

$$m = 2, \tag{23}$$

$$k = \alpha_S G \sqrt{\frac{3b_S}{L_S \bar{M}}}, \tag{24}$$

$$l = (\alpha_G/\alpha_S)^2 (b_G/b_S) L_S \bar{M} \bar{r}. \tag{25}$$

Rewriting Eq. (24) for $L_S \bar{M}$ and substituting the result in Eq. (25), results in the following expression for the material intrinsic length parameter l:

$$l = 3\alpha_G^2 b_G \bar{r} \left(\frac{G}{k}\right)^2. \tag{26}$$

Equation (26) implies that the length scale parameter may vary with strain rate and temperature for the case of $k = \hat{k}(\dot{p}, T)$ with $\dot{p} = \sqrt{2\dot{\varepsilon}_{ij}^p \varepsilon_{ij}^p/3}$.

4 Identification of the material intrinsic length scale from micro hardness tests

Using the gradient plasticity theory, Voyiadjis and Abu Al-Rub [9] and Abu Al-Rub and Voyiadjis [1] derived a framework of equations that can be used to identify the material intrinsic length parameter from microhardness tests. This framework will be treated in this section.

In order to ascertain an expression for the GND density, consider the indentation of a sample by a rigid cone, as shown schematically in Fig. 4.

Evaluating Fig. 4 an expression for w as a function of r can be derived:

$$w(r) = r \tan\theta - \text{h} \quad \text{for } 0 \le r \le a, \tag{27}$$

where h is the indentation depth and θ is the angle between the surface of the conical indenter and the surface of the specimen. For Berkovich indenters one has $\theta = 0.358$.

In this analysis it is assumed that the GND density is integrated by the geometry of the indenter and that the indentation is accommodated by circular loops of GNDs with Burgers vectors normal to the plane of the surface. These deformation loops are visualized schematically in Fig. 5. It is assumed that the deformation loops are being spaced equally along the indentation surface, separated by the individual slip step distance L_G.
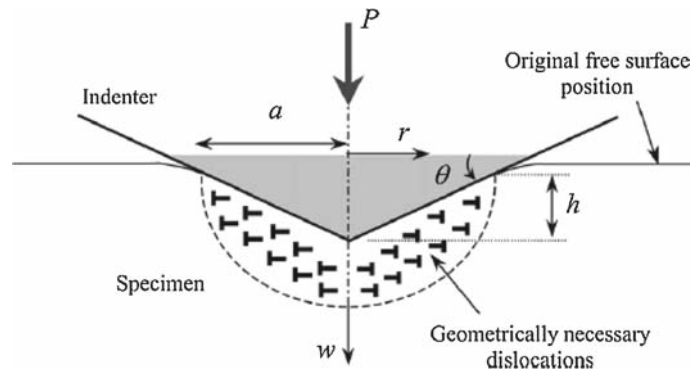

Fig. 4 Specimen being indented by a rigid conical indenter. GNDs created during the indentation process and important geometrical parameters are shown [9]
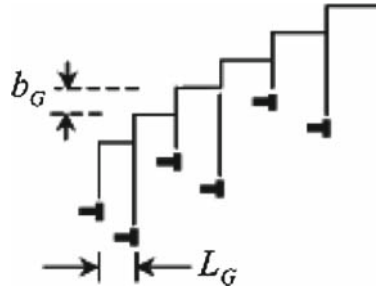
Fig. 5 Deformation loops created during indentation process. L_G is the mean spacing between individual slip steps on the indentation surface [1]

Evaluating Figs. 4 and 5, the following expressions can be obtained:

$$\tan \theta = \frac{h}{a}, \tag{28}$$

$$\left| \frac{dw}{dr} \right| = \frac{b_G}{L_G} = \tan \theta. \tag{29}$$

Substituting Eq. (28) into Eq. (29) and rearranging for L_G yields:

$$L_G = \frac{b_G a}{h}. \tag{30}$$

If λ is the total length of the injected dislocation loops, then an infinitesimal small distance $d\lambda$ can be defined between r and dr:

$$d\lambda = 2\pi r \frac{dr}{L_G} = 2\pi r \frac{h}{b_G a} dr. \tag{31}$$

Integrating this expression from 0 to a and using Eq. (28) yields the total length of dislocation loops λ as

$$\lambda = \int_0^a 2\pi r \frac{h}{b_G a} dr = \frac{\pi a h}{b_G} = \frac{\pi \tan \theta}{b_G} a^2 = \frac{\pi}{b_G} \frac{h^2}{\tan \theta}. \tag{32}$$

During indentation the injected dislocation loops reside in a hemispherical volume V. This volume scales with the contact radius a around the indentation profile. Using Eq. (28) the volume can be defined as

$$V = \frac{2}{3} \pi a^3 = \frac{2}{3} \pi \frac{h^3}{\tan^3 \theta}. \tag{33}$$

Finally, using Eqs. (32) and (33), an expression for the GND density can be derived as follows:

$$\rho_G = \frac{\lambda}{V} = \frac{3}{2} \frac{\tan^2 \theta}{b_G h}. \tag{34}$$

The mapping from the hardness–indentation depth curve (H–h curve) to the tensile stress–plastic strain curve (σ–p curve) is described by Tabor [10]:

$$H = \kappa \sigma, \tag{35}$$

$$p = c \frac{h}{a} = c \tan \theta, \tag{36}$$

where κ is Tabor's factor with a value of $\kappa = 2.8$ [10] and c a material constant in the order of $c = 1$ [11].

Substituting Eqs. (25) and (36) into Eq. (19) and rewriting the result for ρ_S yields the following expression for the SSD density:

$$\rho_S = \frac{c \bar{r} \alpha_G^2 b_G \tan \theta}{l b_S^2 \alpha_S^2}. \tag{37}$$

Furthermore, substituting Eqs. (12) and (13) into Eq. (35) through the use of $\sigma = \sqrt{3}\tau$ yields the following expression for the hardness:

$$H = \sqrt{3}\kappa\alpha_S Gb_S \left[\rho_S^{\beta/2} + (\alpha_G b_G/\alpha_S b_S)^\beta \rho_G^{\beta/2} \right]^{1/\beta}. \tag{38}$$

It is also possible to define the macro-hardness H_0. This is the hardness experienced at greater indentation depths, where there are no size effects. That is in the absence of strain gradients (and thus GNDs), there is solely interaction between SSDs:

$$H_0 = \sqrt{3}\kappa\tau_S = \sqrt{3}\kappa\alpha_S Gb_S \sqrt{\rho_S}. \tag{39}$$

In order to determine the material intrinsic length scale from microindentation experiments the ratio $(H/H_0)^\beta$ is defined. Substituting Eqs. (38) and (39) in this ratio and simplifying the result under the assumption that $\alpha_S = \alpha_G$ and $b_S = b_G$ yields:

$$\left(\frac{H}{H_0}\right)^\beta = 1 + \left(\frac{\rho_G}{\rho_S}\right)^{\beta/2}. \tag{40}$$

Finally, substituting Eqs. (34) and (37) in Eq. (40) and simplifying under the assumption that $\alpha_S = \alpha_G$ and $b_S = b_G$, the following expression is obtained:

$$\left(\frac{H}{H_0}\right)^\beta = 1 + \left(\frac{h^*}{h}\right)^{\beta/2}, \tag{41}$$

$$\text{with} \quad h^* = \zeta l, \tag{42}$$

$$\text{and} \quad \zeta = \frac{3\tan\theta}{2c\bar{r}}. \tag{43}$$

Here h^* is a material specific parameter that characterizes the depth dependence of the hardness and depends on the indenter geometry as well as on the plastic flow.

Furthermore, substituting Eqs. (26) and (37) into Eq. (39) yields a simpler expression for the macro-hardness H_0, which is more convenient to use in determining the material intrinsic length scale:

$$H_0 = \kappa k \sqrt{c\tan\theta}, \tag{44}$$

where k can be obtained from Eq. (24). Equation (42) shows that h^* a linear function of l. Therefore, in order to determine the material intrinsic length scale l, it is important to determine a value for h^*. Now the usage of the indentation experiments comes into play. The experiments yield a data pool of hardness values as a function of indentation depth. Plotting the data as $(H/H_0)^\beta$ versus $h^{-\beta/2}$ and fitting a linear function on the data, yields a straight line with slope $h^{*\beta/2}$. Combining this slope with Eqs. (42) and (43), a constant value for the material intrinsic length scale can be determined.

5 Inclusion of the hardening effect into the standard gradient plasticity formulation

The hardening effect described in Sect. 1 and visualized in Fig. 2 was addressed by Almasri and Voyiadjis [4]. They performed nanoindentation tests on several metal samples with high surface roughness and though the presence of the effect significantly differed for the different samples, the effect was encountered in all of them.

They established a framework of empirical expressions for the hardness H as a function of indentation depth h, that can be used to fit on the results of the nanoindentation experiments [4]:

$$H = \begin{cases} H_1 + l_1 h^{-n1}, & h < h_1, \\ H_2 \left(l_2 - e^{-n_2 h}\right), & h_1 < h < h_2, \\ H_3 + l_3 h^{-n3}, & h > h_2. \end{cases} \tag{45}$$

In these equations the subscripts 1, 2 and 3 indicate the initial decrease in hardness zone, the increase in hardness zone and the final decrease in hardness zone, respectively. Furthermore, l_i and n_i are material parameters acquired from the fitting process.
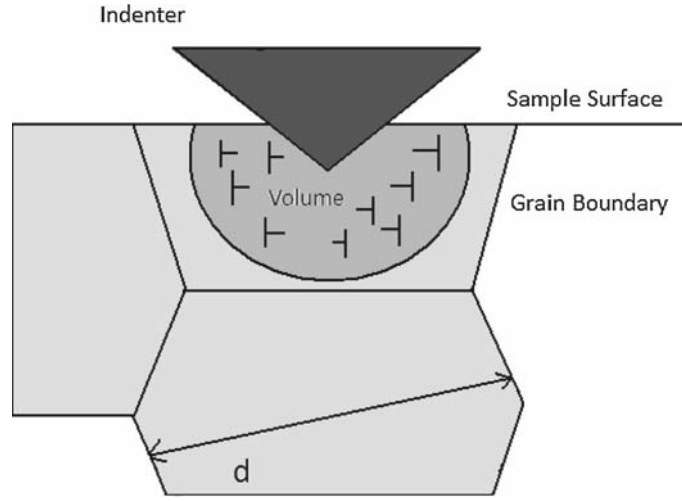
Fig. 6 The expansion of the plastic zone V is obstructed by the grain boundary. Due to ongoing indentation the GND density increases, resulting in an increase in hardness

This empirical framework yields nice fits for the experimental results, however, it does not provide a physical background for the justification of these relations and the underlying physics of the problem.

In the proposed work presented here an attempt is made to address the physical justification of the relations that described such a behavior. A new expression for H as a function of h is derived, based on a solid physical background.

Other researchers have also encountered the hardening/softening effect in nanoindentation experiments [12]. It is believed that the hardening effect arises due to the interaction between GNDs and grain boundaries. As described in Sect. 2, during indentation the GNDs will accumulate in an expanding plastic zone, the hemispherical volume V. At a certain point, the boundary of this plastic zone will reach a grain boundary. Upon reaching the grain boundary the plastic zone will stop expanding because it is obstructed by this grain boundary. However, due to the ongoing indentation new GNDs are still being created inside the plastic zone, causing the GND density to increase. As a result of this increase in GND density there will be more interaction between the GNDs amongst themselves and between the GNDs and the grain boundary. This ultimately leads to an increase in the local hardness of the material. This is visualized in Fig. 6.

The key to defining a new expression for the hardness is to define a new relation for the GND density ρ_G, using the events described above as a sound physical background.

Recalling the definition of the GND density from Eq. (34) it can be seen that ρ_G depends on the total length of dislocation loops λ and the volume of the plastic zone V. For this case the expression for λ remains unchanged. However, the expression for the volume V needs to be updated.

The volume V of the plastic zone, upon reaching the grain boundary, is defined by

$$V = \frac{\pi}{12}d^3, \tag{46}$$

with d the grain size. In addition, it can be seen in Fig. 6 that a certain portion of the plastic zone volume is taken up by the indenter. This volume V_{indent} is given by:

$$V_{\text{indent}} = \varphi h^3, \tag{47}$$

where φ is a geometrical constant.

The shape of V_{indent} is pyramidal. The volume of a pyramid is given by:

$$V_{\text{pyramid}} = \frac{1}{3}A_{\text{base}}h, \tag{48}$$

with h the height of the pyramid, which in this case is the depth of indentation. A_{base} can be deduced from the area function of an ideal Berkovich indenter:

$$A_{\text{base}} = 24.56h^2, \tag{49}$$

with h the indentation depth. Substituting this relation in Eq. (48) yields:

$$V_{\text{indent}} = 8.19h^3. \tag{50}$$

Comparing this with Eq. (47) it follows that $\varphi = 8.19$.

Using these results the volume of the plastic zone can be defined as follows:

$$V_{\text{plastic}} = V - V_{\text{indent}} = \frac{\pi}{12}d^3 - 8.19h^3. \tag{51}$$

With this new definition for the volume of the plastic zone, it is possible to define a new expression for the GND density ρ_G using Eqs. (32), (51) and (12):

$$\rho_G = \frac{\lambda}{V_{\text{plastic}}} = \frac{\frac{\pi}{b_G}\frac{h^2}{\tan\theta}}{\frac{\pi}{12}d^3 - 8.19h^3} = \frac{h^2}{b_G \tan\theta \left(\frac{1}{12}d^3 - 8.19h^3\right)}. \tag{52}$$

Making use of this result for ρ_G it is possible to redefine the ratio $(H/H_0)^\beta$ using Eq. (40):

$$\left(\frac{H}{H_0}\right)^\beta = 1 + \left(\frac{lh^2}{\left(\frac{1}{12}d^3 - 8.19h^3\right)c\bar{r}\tan^2\theta}\right)^{\beta/2}. \tag{53}$$

In this equation, the material length scale is a constant. However, Voyiadjis and Abu Al-Rub [13] have introduced a variable material length scale:

$$l = \bar{M}\bar{r}\left(\frac{Dd}{D + dp^{1/m}}\right), \tag{54}$$

with D the size of the sample, d the grain size and p the plastic equivalent strain. The plastic equivalent strain depends on the indentation depth, thus making l variable.

Substituting this expression in Eq. (53) yields:

$$\left(\frac{H}{H_0}\right)^\beta = 1 + \left[\frac{\bar{M}h^2}{\left(\frac{1}{12}d^3 - 8.19h^3\right)c\tan^2\theta}\left(\frac{Dd}{D + dp^{1/m}}\right)\right]^{\beta/2}. \tag{55}$$

6 Sample preparation

Five different samples are being tested in this work. They are all metal slug samples.

The indentations are performed on the top, flat surface of each sample. These surfaces are not smooth in their standard form. In order to require reliable results from the tests, it is necessary to polish the indentation surface of each of these samples. During one test 16 indentations are performed in a 4×4 array. In order to ensure consistency amongst the 16 indentations it is of the utmost importance that the surface is as smooth as possible. It is easy to realize that the result for each indentation will differ significantly from other indentations for a high surface roughness. This is due to a completely different surface topography for each indentation.

The samples are polished in several steps using grindstones with different grid grades. First the samples are encapsulated in epoxy. This increases the surface that is being pressed on to the grindstone and minimizes wobbling of the sample to ensure a flat sample. First a rough grindstone is used to expose the sample surface by removing the epoxy layer above it. Following that, two glass plates are sprinkled with a mixture of 800 and 1,000 grid respectively. The sample is grinded on both plates until a relatively smooth, shiny surface is reached. The final step is to fine-polish the sample using a grindstone with a 1,200 grid mixture sprinkled on it.

To check the difference in surface roughness, scanning electron microscope (SEM) images of the surface were made before (Fig. 7) and after polishing (Fig. 8). It can be clearly seen that the roughness has decreased significantly and just some small surface defects are remaining.
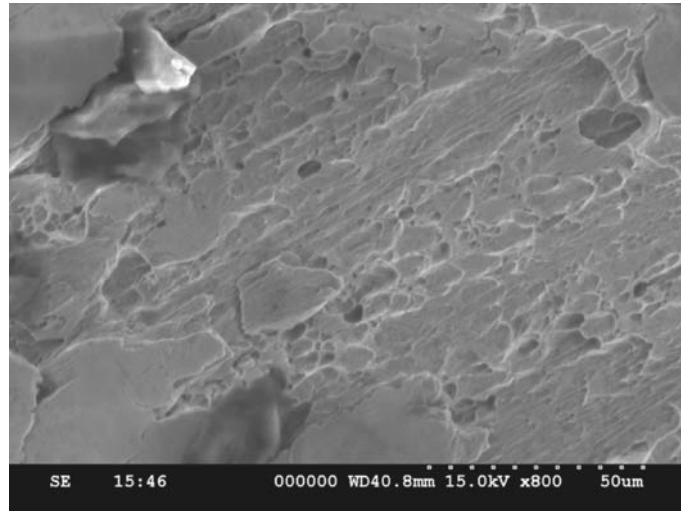
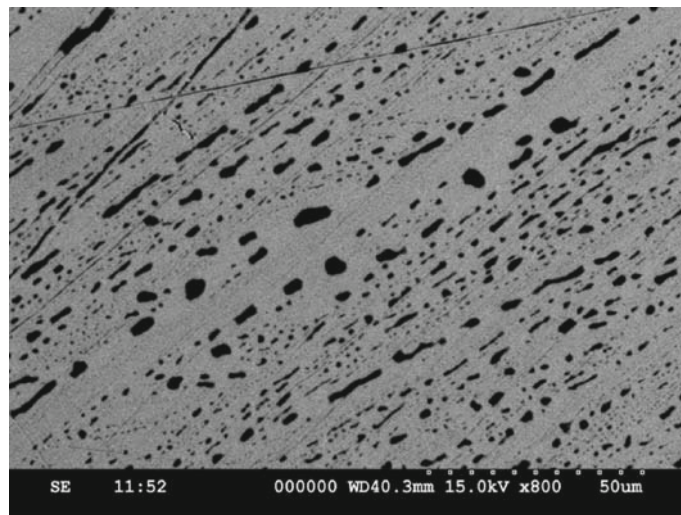**Fig. 7** SEM image of Copper 1 surface before polishing

Fig. 8 SEM image of Copper 1 surface after polishing

7 Experimental results

The main goal of the experimental part is to reproduce the experiments performed by Almasri and Voyiadjis [4] and obtain a physical model to describe this behavior. It is vital to investigate particularly the behavior of the increase in hardness with increasing indentation depth (for small depths) that was encountered in the experiments of Almasri and Voyiadjis [4]. However, it should be noted that those samples were not polished. A typical result of these experiments can be seen in Fig. 9 [4]. The tested samples and properties are indicated in Table 1.

The results encountered in the experiments performed for this work using polished samples show the same trend. The results for copper 1 (99.9960% purity) can be seen in Fig. 10.

The results for copper 2 (99.9999% purity) can be seen in Fig. 11.

The results for aluminum 1 (99.9900% purity) can be seen in Fig. 12.

The results for aluminum 2 (99.9999% purity) can be seen in Fig. 13.

The results for nickel (99.9995% purity) can be seen in Fig. 14.

It can be seen from these figures that especially the two copper samples exhibit this hardening behavior very strongly.
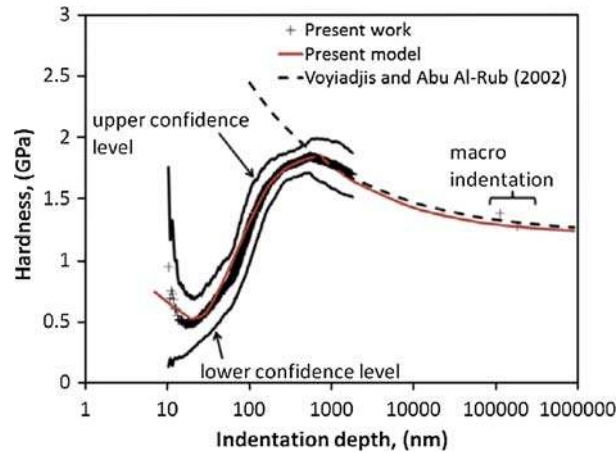
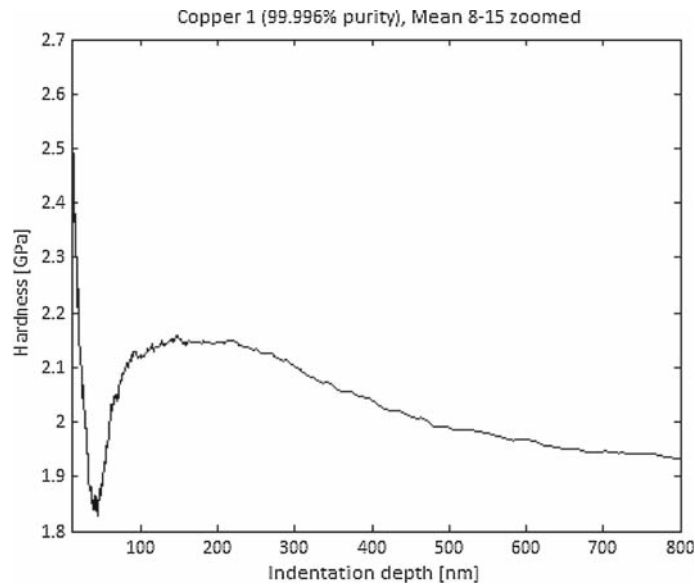**Fig. 9** Indentation depth versus hardness for Copper 2 (99.9999% purity) [4]

Fig. 10 Results for copper 1 (99.9966% purity)

The aluminum 1 sample has a very short hardening segment, whereas the aluminum 2 sample does not seem to have any hardening segment. This curve is a typical example of the classical ISE.

Finally, the nickel sample shows a hardening segment. However, following that the hardness remains more or less the same, without going down to lower values, as can be seen for both of the copper samples.

Apparently there are some differences in the way the dislocations interact with the grain boundaries for each of the metals.

Another trend that can be observed from the figures is that when the purity grade of a metal increases, the macro-hardness of this metal decreases. This can be explained by looking at the dislocation density. The less pure a metal is, the more dislocations there will be and thus the dislocation density will be higher. This implies that there are more interactions between the dislocations, thus increasing the hardness of the metal.

To see if the polishing of the surfaces had a positive effect on the experiments, the current experiments are compared to the experiments performed by Almasri and Voyiadjis [4]. In [4], the experiments were performed on samples that were not polished. Tables 2 and 3 list the mean, the standard deviation and the coefficient of variation (COV) for the elasticity modulus and the hardness, respectively, as calculated by the MTS Nano-indenter XP for the arrays of tests. It is important to mention that the experiments for the polished and unpolished state were performed on the same kind of metal slug samples.
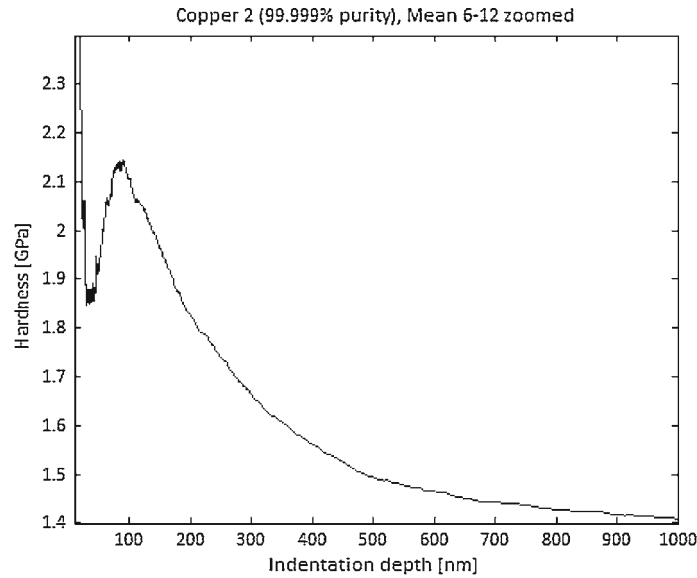
Fig. 11 Results for copper 2 (99.9999% purity)
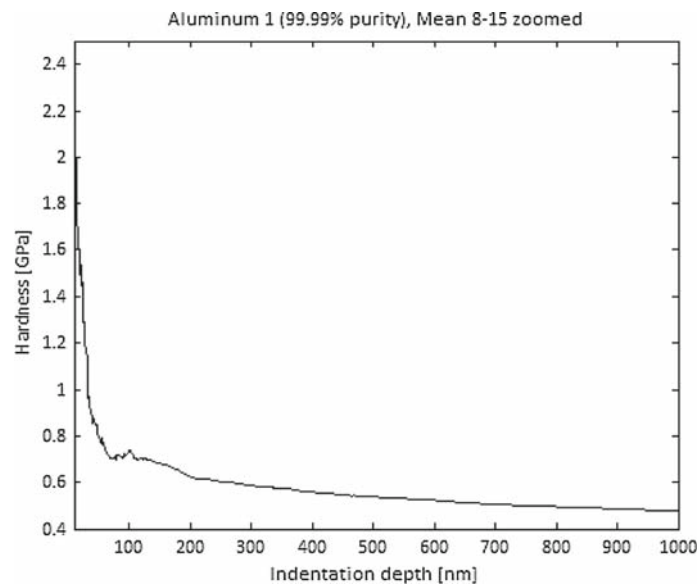

Fig. 12 Results for aluminum 1 (99.9900% purity)

These tables clearly indicate that the consistency of the current experiments is better than it is for the experiments performed by Almasri and Voyiadjis [4].

Figures 15, 16, 17, 18 and 19 provide a graphical representation of the differences between the current experiments and the experiments performed by Almasri and Voyiadjis [4].

It is observed that the unpolished samples exhibit lower modulus of elasticity as shown in Table 2. Table 3 shows that most of the polished samples exhibit higher hardness values. Furthermore, the unpolished samples exhibit considerably higher percentages in COV. In Fig. 15, one notes that the hardness is considerably lower in the unpolished case for copper 1. In Fig. 16, one notes that in the case of copper 2 lower hardness is exhibited at smaller indentation depths (less than 200 nm), however, at higher depths the hardness keeps increasing contrary to real expectations of the material behavior. It eventually levels off and maintains a constant value for the hardness. The same observations as above are exhibited in Figs. 18 and 19 for Aluminum 2 and Nickel,
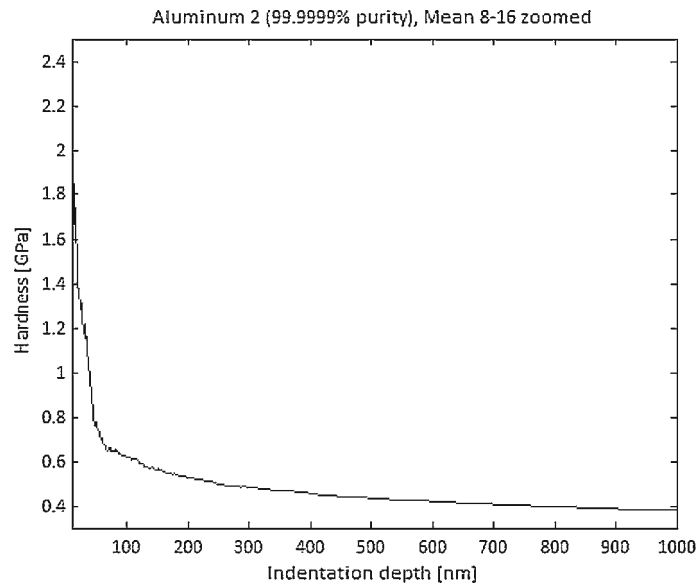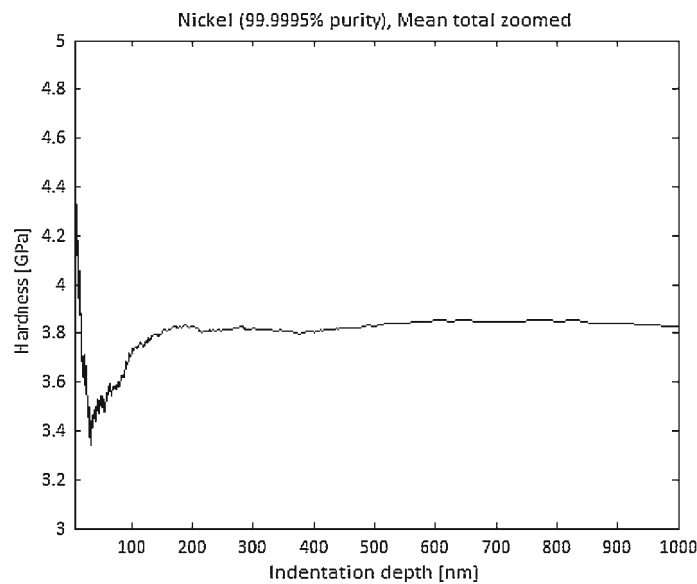
Fig. 13 Results for aluminum 2 (99.9999% purity)

Fig. 14 Results for nickel (99.9995% purity)

Table 1 Tested samples and their properties

| Sample	Sample type	Purity (%)	Dimensions (diameter × height)
Copper 1	Slug	99.9960	6.35 mm × 12.7 mm
Copper 2	Slug	99.9999	6.35 mm × 12.7 mm
Aluminum 1	Slug	99.9900	6.35 mm × 12.7 mm
Aluminum 2	Slug	99.9999	6.35 mm × 12.7 mm
Nickel	Slug	99.9950	6.35 mm × 12.7 mm

respectively. In the case of Aluminum 1 as shown in Fig. 17 there seems to be no significant difference in variation of hardness between the polished and unpolished samples, except at extremely low indentations of the order of 20 nm.

Table 2 Qualitative comparison of the elasticity modulus for the current experiments and the experiments performed by Almasri and Voyiadjis [4]

Sample	Current mean E (GPa)	Almasri and Voyiadjis mean E (GPA)	Current standard deviation E (GPa)	Almasri Voyiadjis standard deviation E (GPa)	Current COV (%) E	Almasri and Voyiadjis COV (%) E
Copper 1	138.19	108.075	3.426	46.986	2.48	43.48
Copper 2	135.265	105.646	2.692	16.385	1.99	15.51
Aluminum 1	70.656	58.114	2.256	6.602	3.19	11.36
Aluminum 2	66.247	55.06	4.125	24.685	6.23	44.83
Nickel	236.573	148.843	3.628	69.285	1.53	46.55

Table 3 Qualitative comparison of the hardness for the current experiments and the experiments performed by Almasri and Voyiadjis [4]

Sample	Current mean H (GPa)	Almasri and Voyiadjis Mean H (GPA)	Current standard deviation H (GPa)	Almasri and Voyiadjis standard deviation H (GPa)	Current COV (%) H	Almasri and Voyiadjis COV (%) H
Copper 1	1.928	1.779	0.091	0.849	4.700	47.69
Copper 2	1.468	1.467	0.078	0.343	5.330	23.39
Aluminum 1	0.489	0.702	0.051	0.233	10.46	33.20
Aluminum 2	0.410	0.280	0.044	0.153	10.77	54.70
Nickel	3.834	2.636	0.081	2.225	2.120	84.39
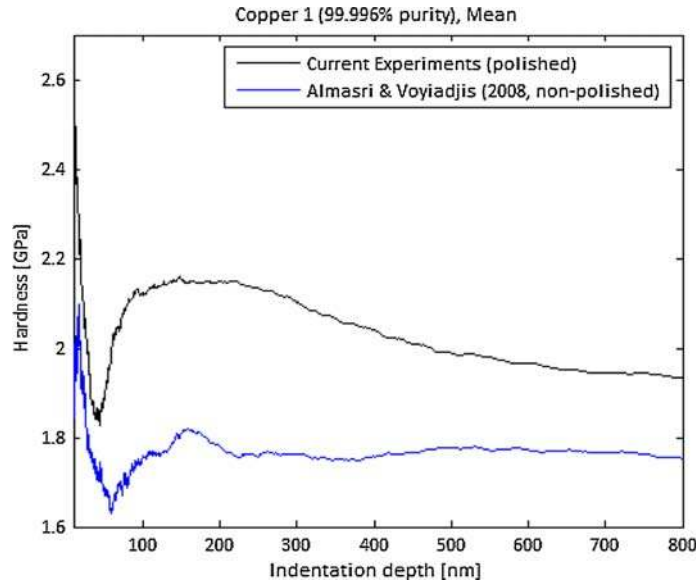
Fig. 15 Experiments compared for copper 1 (99.996% purity)

8 Comparison of the experimental results with the developed models

In this section the experimental results presented from the previous section are compared with the model proposed by Voyiadjis and Abu Al-Rub [9] and the model developed in Sect. 4 (Eq. 55). Rewriting Eq. (55) for H yields

$$H = H_0 \left[1 + \left[\frac{\bar{M}h^2}{\left(\frac{1}{12}d^3 - 8.19h^3\right)c\tan^2\theta} \left(\frac{Dd}{D + dp^{1/m}} \right) \right]^{\beta/2} \right]^{1/\beta}. \tag{56}$$
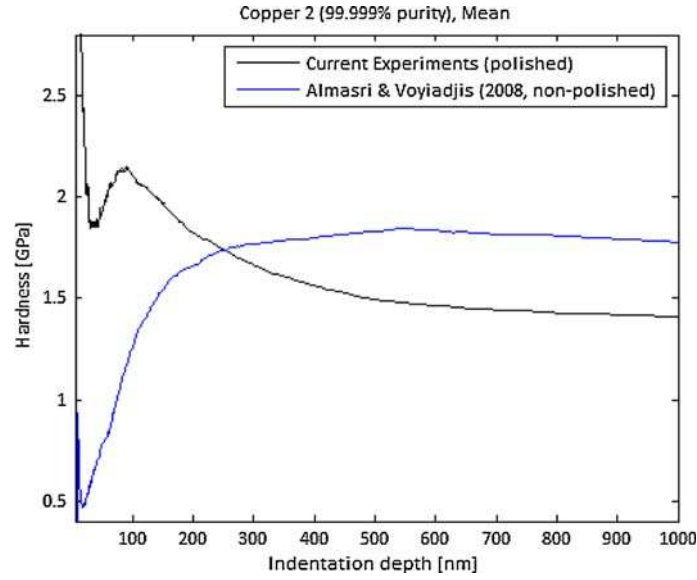
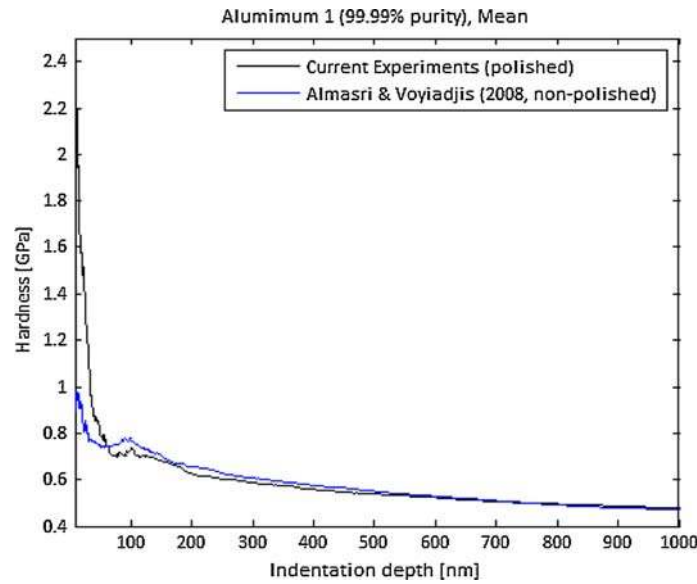**Fig. 16** Experiments compared for copper 2 (99.999% purity)

Fig. 17 Experiments compared for aluminum 1 (99.99% purity)

To be able to fit this expression to the experimental results, four material parameters are introduced: $\alpha_1, \alpha_2, \alpha_3$ and h_1. This modifies Eq. (56) into the following expression:

$$H = \alpha_1 H_0 \left[1 + \left[\frac{\alpha_2 \bar{M}(h - h_1)^2}{\left(\frac{\alpha_3}{12} d^3 + 8.19(h - h_1)^3 \right) c \tan^2 \theta} \left(\frac{Dd}{D + dp^{1/m}} \right) \right]^{\beta/2} \right]^{1/\beta}. \tag{57}$$

Furthermore, the minus sign in the denominator is changed into a plus sign to mirror the graph along the y-axis. All the variables in Eq. (57) are known, except for the plastic equivalent strain p, which is a function of the indentation depth: $p = p(h)$.

The plastic equivalent strain is determined by performing numerical analysis with ABAQUS as will be described in Sect. 8.

Furthermore, it is necessary to introduce an expression which can be used to bend the graph up or down for bigger indentation depths. This is done by using an expression developed by Voyiadjis and Abu Al-Rub [14],
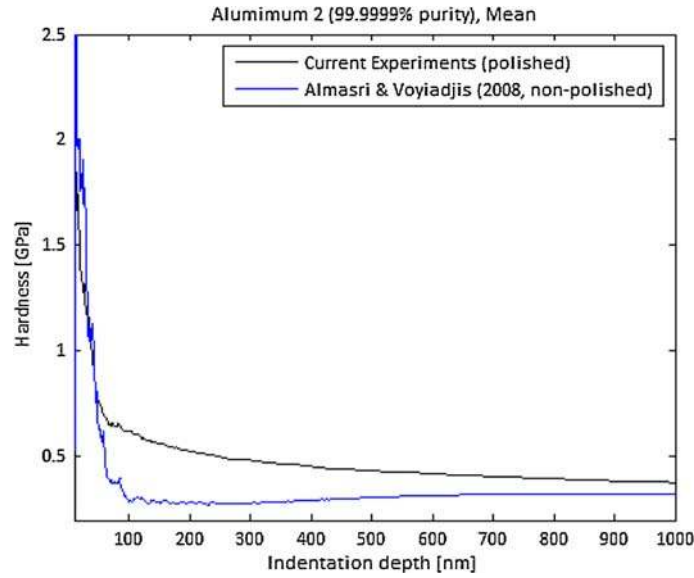
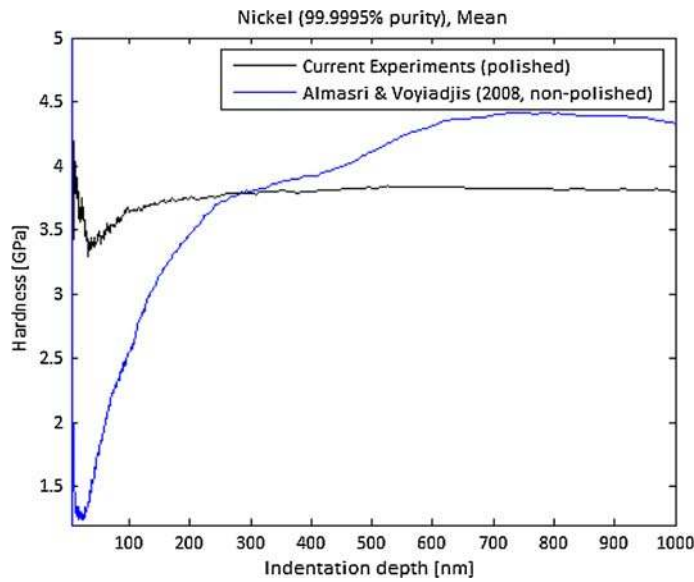**Fig. 18** Experiments compared for aluminum 2 (99.9999% purity)

Fig. 19 Experiments compared for nickel (99.9995% purity)

which is based on the work by Armstrong and Frederick [15], Phillips et al. [16] and Chaboche and Rousselier [17]:

$$X_{ij} = \sum_{k=1}^{M} C^{(k)} X_{ij}^{(k)}. \tag{58}$$

Combining this with Eq. (57) and summing over $M = 2$ terms yields

$$H = H + C(h)H \tag{59}$$

with

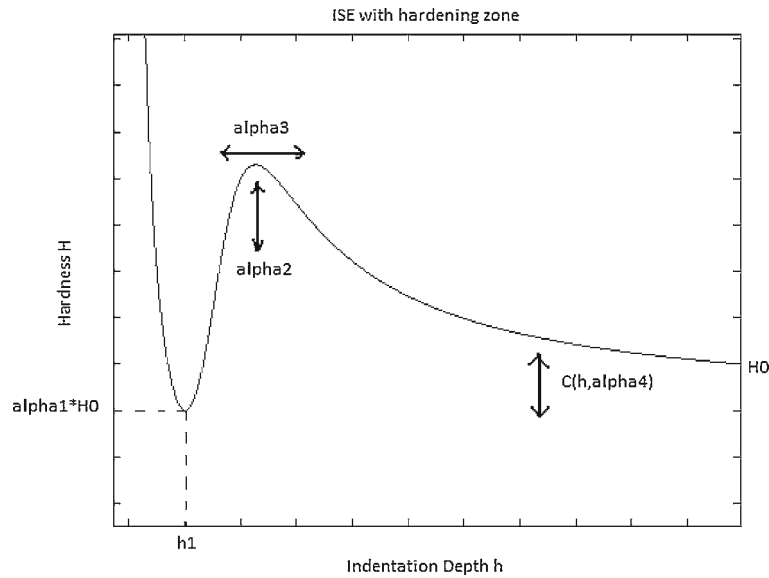$$C(h) = C(h, \alpha_4) = \sqrt{\frac{h}{\alpha_4}}. \tag{60}$$

Fig. 20 Influence of the material parameters from Table 2 on the shape of the graph

Table 4 The material parameters used to fit Eq. (59) to the experimental results

Sample	H_0 (GPa)	h_1 (nm)	$\alpha_1[-]$	$\alpha_2[-]$	$\alpha_3[-]$	$\alpha_4[-]$	Sign $C(h, \alpha_4)$
Copper 1	1.8911	40	1.079	0.0030	4.8×10^{-4}	300,000	−
Copper 2	1.3639	42.5	1.408	0.0050	6.0×10^{-4}	20,000	−
Aluminum 1	0.4460	80	1.861	0.0008	3.6×10^{-4}	6,000	−
Aluminum 2	0.3519	80	2.074	0.0008	3.0×10^{-4}	5,000	−
Nickel	3.7555	40	0.895	0.0080	0.0102	100,000	+

By taking the sign of $C(h)$ to be positive or negative and by varying α_4, the bending of the graph can be influenced to fit the experimental results.

Figure 20 demonstrates how $\alpha_1, \alpha_2, \alpha_3, \alpha_4, h_1$ and $C(h)$ can be used to fit Eq. (59) to the experimental results.

Table 4 gives the values of the parameters used in the fitting process.

Using these parameters, the models fitted to the experimental results are shown in Figs. 21, 22, 23, 24 and 25. Furthermore the following values are used: $\bar{M} = 0.5, d = 1,000$ nm, $c = 1, \theta = 0.358, D = 50$ μm (same as in the ABAQUS simulation), $m = 0.474$ [18] and $\beta = 2$. The functions used for p will be outlined in Sect. 8.

In Figs. 21, 22, 23, 24 and 25, Voyiadjis and Peters (2009) indicate the present formulation for hardness adopted by the authors and proposed in this paper.

It can be concluded from these figures that the newly developed model provides a good description of the ISE when a strong hardening effect is present. This can be seen in Figs. 21 and 22 for copper 1 and copper 2.

However, if the hardening effect is weak, the model developed by Voyiadjis and Abu Al-Rub [2] is better suited to describe the ISE. This can be seen in Figs. 23 and 24 for aluminum 1 and aluminum 2. These figures display the results that are more like the classical ISE.

The results for nickel in Fig. 25 also show a strong hardening effect. However, after the increase in hardness, there is no subsequent decrease in hardness, but instead hardness more or less remains constant. The newly developed model is suited to describe the hardening region, but the description of both softening regions is less accurate.

9 Numerical simulation using ABAQUS

As mentioned in the previous sections, it is necessary to simulate the indentation problem using a Finite Element Package. The goal is to determine the plastic equivalent strain as a function of the indentation depth. The commercial Finite Element Package used here is ABAQUS.
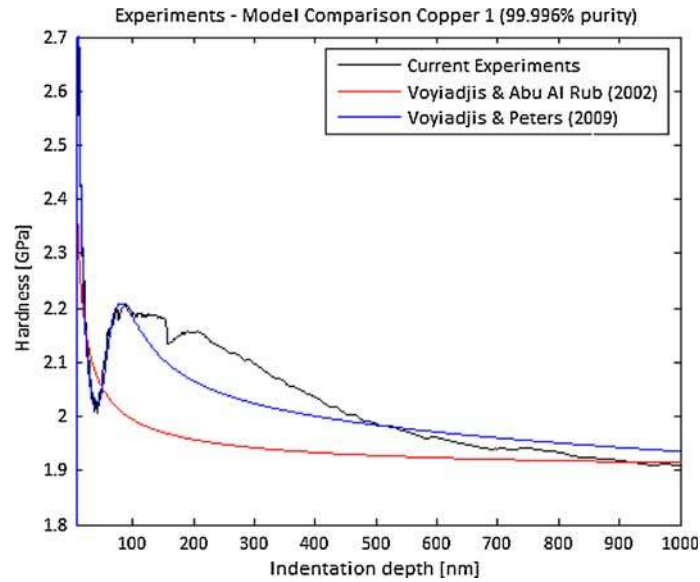
Fig. 21 Models fitted to the experimental results of the copper 1 sample in indentation
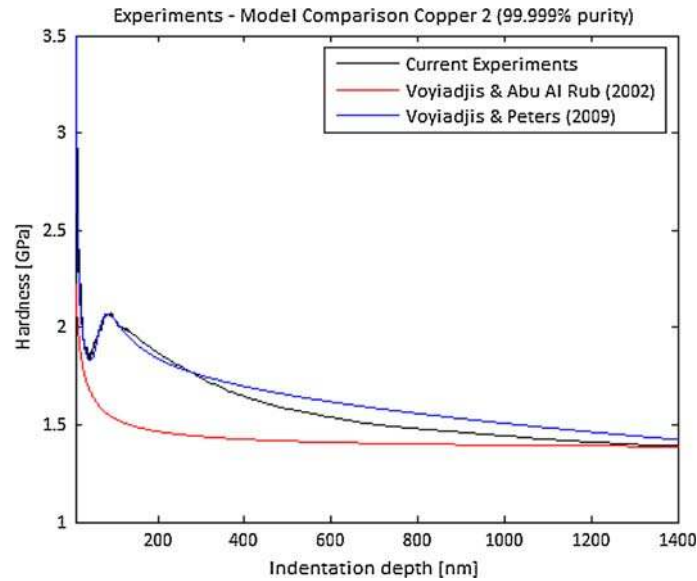

Fig. 22 Models fitted to the experimental results of the copper 2 sample in indentation

A cube with dimensions of $D = 50\ \mu$m is modeled to represent a small piece of the sample. The Berkovich indenter is modeled on top of the cube and is modeled as a blunt pyramid. The tip of the indenter is an equilateral triangle with sides that measure 20 nm. ABAQUS' interaction module is used to model the contact between the indenter and the sample (Fig. 26).

A vertical line of symmetry with respect to the indenter is assumed and the corresponding boundary conditions are developed based on this line of symmetry. A rate-dependent finite element formulation is used to alleviate mesh dependence. However, in future work the authors will also incorporate a gradient finite element formulation (developed in previous work by the first author) to ensure a more robust solution. Assigning a certain velocity (see Table 5) to the indenter causes it to penetrate the sample to a depth of around 2,000 nm, just as in the experiments. After that plastic deformation takes place an indent can be seen at the sample surface.

Figure 27 shows the deformation of the sample surface after indentation. Clearly visible are the pile-up regions at the sides of the indent. This is some of the material that originally occupies the indent space. It has been pushed outwards by the indenter. This is due to high indentation occurring in a small vicinity that allows
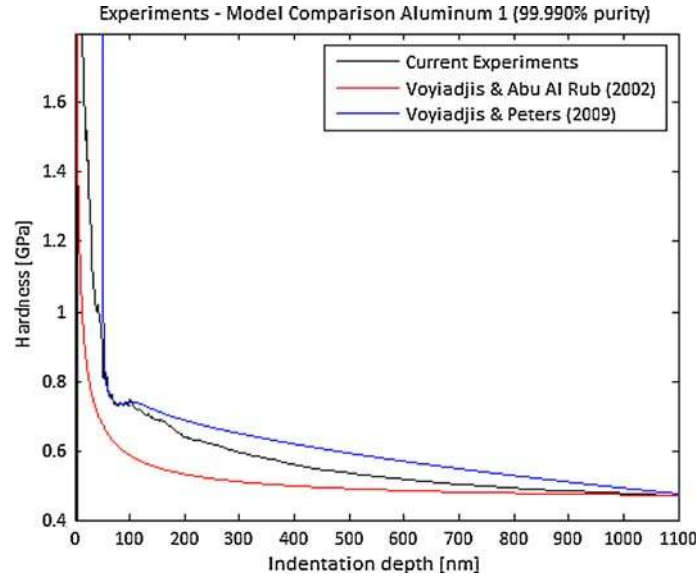
Fig. 23 Models fitted to the experimental results of the aluminum 1 sample in indentation
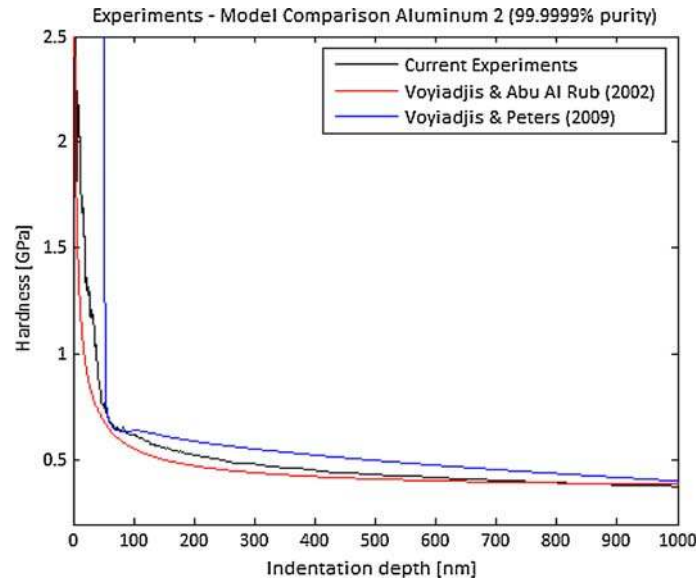

Fig. 24 Models fitted to the experimental results of the aluminum 2 sample in indentation

the material to pile-up at the periphery of the indenter. The pile-up effect can also be seen in Fig. 28, which shows the sample surface after indentation as viewed through the microscope in the MTS Nanoindenter XP.

ABAQUS can be used to calculate the plastic equivalent strain as a function of the indentation depth, which is needed to plot Eq. (59).

ABAQUS' output shows the plastic equivalent strain as a linear function of the indentation depth. The results for the different samples can be seen in Table 5.

Observing from Sects. 2 and 3 and substituting Eqs. (15) and (19) in Eq. (40), an alternative expression can be derived for the hardness ratio:

$$\left(\frac{H}{H_0}\right)^{\beta} = 1 + \left(\frac{\eta \bar{r} b_S L_S \bar{M}}{p b_G}\right)^{\beta/2} = 1 + \left(C \frac{\eta}{p}\right)^{\beta/2}, \tag{61}$$
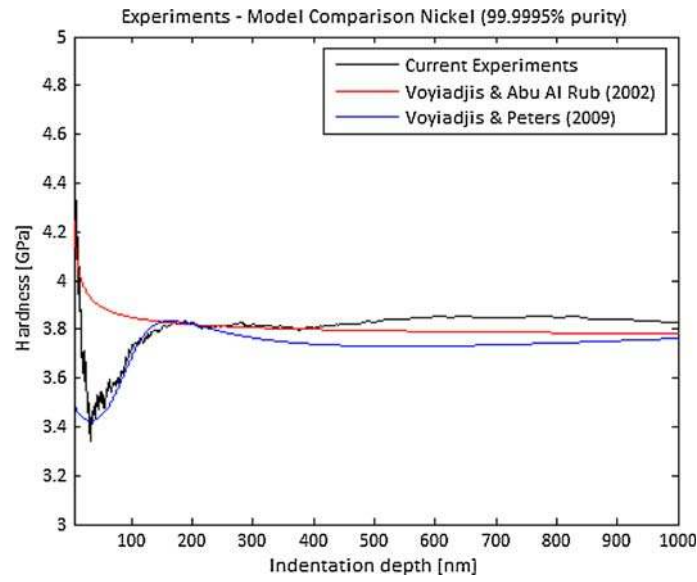
Fig. 25 Models fitted to the experimental results of the nickel sample in indentation
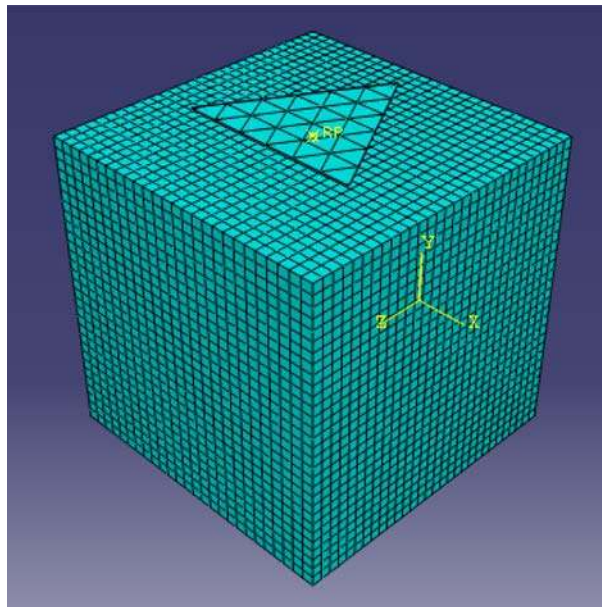

Fig. 26 Indenter and sample modeled and meshed in ABAQUS

Table 5 ABAQUS simulation properties and results

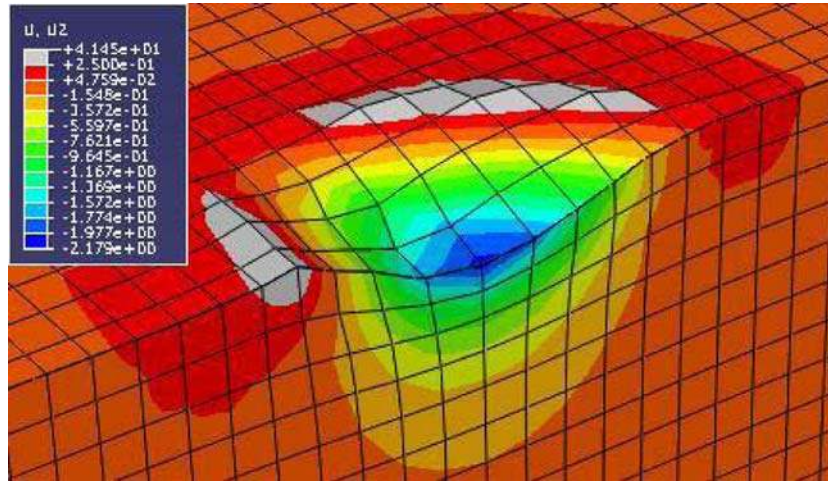| Sample	Vertical speed of indenter (m/s)	p (h)	Final p after indentation (%)
Copper 1	−2	4.137×10^{-4}	90.60
Copper 2	−2	4.1708×10^{-4}	90.34
Aluminum 1	−2	3.417×10^{-4}	66.96
Aluminum 2	−2	3.4956×10^{-4}	67.44
Nickel	−1.7	3.1203×10^{-4}	60.20

Fig. 27 Vertical displacement in a contour plot cut after indentation. The grey areas are pile-up regions. Values in the legend are in μm
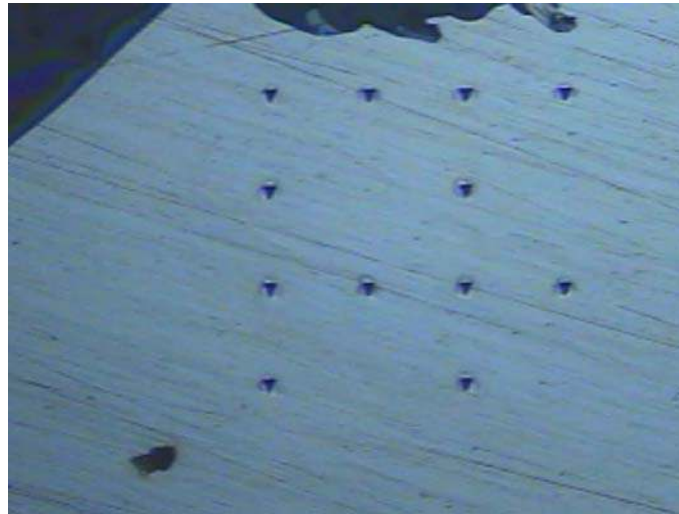

Fig. 28 Copper 2 sample surface after indentation. Pile-up regions can be seen at the edges of the indents

with

$$C = \frac{\bar{r} b_S L_S \bar{M}}{b_G}.$$ (62)

Besides providing the plastic equivalent strain p, ABAQUS can be used to acquire the gradient of the plastic equivalent strain η. The parameter C then describes the microstructure of the material. However, to obtain the gradient it is necessary to incorporate a material model within ABAQUS that simulates the material behavior as described in Sect. 4. This is beyond the scope of this work, but is recommended for further studies regarding this subject.

10 Conclusion

Indentation size effects encountered in nanoindentation experiments are addressed in this work. The classical descriptions of the ISE show a decrease in hardness for increasing indentation depth. However, recently new experiments have shown that after the initial decrease, hardness increases with increasing indentation depth. After this increase, finally the hardness decreases with increasing indentation.

The work presented here reviews existing theories describing the ISE and presents new formulations that incorporate the hardening effect into the ISE. Furthermore, indentation experiments have been performed on several metal samples, to see whether the hardening effect was an anomaly or not.

The goal of this work is to ascertain the three regions in hardness during nanoindentation as obtained experimentally [4]. The data presented in this work describes a similar trend, being the hardening effect. Furthermore, the data in this work is proven to be much more consistent and reliable. This can be acknowledged to the fact that the samples used in this work have been thoroughly polished before indenting them.

A new expression for the GND density ρ_G (Eq. 52) is proposed in this work in order to account the changes in the hardening/softening region that appears at the beginning of the indentation process. Making use of this result for ρ_G it is possible to redefine more accurately and physically based the ratio $(H/H_0)^\beta$ (see Eq. (55)) by making use of a variable length scale.

The new model presented in this work can be used to accurately describe the hardening section during indentation especially at small depths. An extensive fitting procedure has been presented to match the model to the data from nanoindentation experiments.

Numerical analysis, using the commercial finite element package ABAQUS, is used to acquire data for the plastic equivalent strain during indentation. Incorporating a material model into ABAQUS that describes the hardening during indentation can provide a more thorough simulation of the problem. This is recommended for further simulation studies regarding nanoindentation.

References

1. Abu Al Rub, R.K., Voyiadjis, G.Z.: Analytical and experimental determination of the material intrinsic length scale of strain gradient plasticity theory from micro- and nano-indentation experiments. Int. J. Plast. **20**(6), 1139–1182 (2004)
2. Voyiadjis, G.Z., Abu Al Rub, R.K.: Length scales in gradient plasticity. In: Ahzi, S., Cherkaoui, M., Khaleel, M.A., Zbib, H.M., Zikry, M.A., LaMatina, B. (eds.): Proceedings of the IUTAM Symposium on Multiscale Modeling and Characterization of Elastic-Inelastic Behavior of Engineering Materials, October 2002, pp. 167–174. Kluwer Academic Publishers, Morocco (2002)
3. Abu Al Rub, R.K., Voyiadjis, G.Z.: A physically based gradient plasticity theory. Int. J. Plast. **22**(4), 654–684 (2006)
4. Almasri, A.H., Voyiadjis, G.Z.: Nanoindentation in FCC metals: experimental study. Acta Mechanica **18** (2009)
5. Lucas, B.N., Oliver, W.C. Phar, G.M., Loubet, J.-L.: Time-dependent deformation during indentation testing. Thin films: Stresses and mechanical properties VI. In: Proceedings of the Symposium, San Francisco, CA, USA, 8–12 Apr 1996, pp. 233–238 (1997)
6. Gao, H., Huang, Y.: Geometrically necessary dislocation and size-dependent plasticity. Scr. Mater. **48**, 113–118 (2003)
7. Nix, W.D., Gao, H.: Indentation size effects in crystalline materials: a law for strain gradient plasticity. J. Mech. Phys. Solids. **46**(3), 411–425 (1998)
8. Arsenlis, A., Parks, D.M.: Crystallographic aspects of geometrically-necessary and statistically stored dislocation density. Acta Mater. **7**(5), 1597–1611 (1999)
9. Voyiadjis, G.Z., Abu Al-Rub, R.K.: Determination of the material intrinsic length scale of gradient plasticity theory. Int. J. Multiscale Comput. Eng. **2**(3), 377–400 (2004)
10. Tabor, D.: The Hardness of Metals. Clarendon Press, Oxford, 1951
11. Xue, Z. et al.: The influence of indenter tip radius on the micro indentation hardness. Eng. Mater. Technol. **124**(3), 371–379 (2002)
12. Yang, B., Vehoff, H.: Dependence of nanohardness upon indentation size and grain size—a local examination of the interaction between dislocations and grain boundaries. Acta Mater. **55**(3), 849–856 (2007)
13. Voyiadjis, G.Z., Abu Al-Rub, R.K.: Gradient plasticity theory with a variable length scale parameter. Int. J. Solids Struct. **42**(14), 3998–4029 (2005)
14. Voyiadjis, G.Z., Abu Al-Rub, R.K.: Thermodynamic Based Model for the Evolution Equation of the Backstress in Cyclic Plasticity, vol. **19**, Issue 12. Elsevier, Baton Rouge (2003)
15. Armstrong, P.J., Frederick, C.O.: A Mathematical Representation of the Multiaxial Bauschinger Effect, vol. **21**, no. 4. Berkeley Laboratories, Berkeley (1966)
16. Phillips, A., Tang, J.L., Ricciuti, M.: Some new observations on yield surfaces. Acta Mech. **20**(1–2), 23–39 (1984)
17. Chaboche, J.-L., Rousselier, G.: On the plastic and viscoplasic constitutive equations, part I: rules developed with internal variables concept. Part II: application of internal variable concepts to the 316 stainless steel. ASME J. Press. Vessel Technol. **105**, 153–158 (1983)
18. Roylance, D. http://web.mit.edu/course/3/3.11/www/modules/ss.pdf. Accessed 23 Aug 2001